

Montana Tech Library

Digital Commons @ Montana Tech

Graduate Theses & Non-Theses

Student Scholarship

Spring 5-4-2024

Using Unmanned Aircraft System (UAS)-borne high-resolution hyperspectral imaging and gamma radiometry for rare earth element exploration in the Bearpaw Mountains, Montana USA

Emma Kamp

Montana Technological University

Follow this and additional works at: https://digitalcommons.mtech.edu/grad_rschr



Part of the [Geological Engineering Commons](#)

Recommended Citation

Kamp, Emma, "Using Unmanned Aircraft System (UAS)-borne high-resolution hyperspectral imaging and gamma radiometry for rare earth element exploration in the Bearpaw Mountains, Montana USA" (2024). *Graduate Theses & Non-Theses*. 312.

https://digitalcommons.mtech.edu/grad_rschr/312

This Publishable Paper is brought to you for free and open access by the Student Scholarship at Digital Commons @ Montana Tech. It has been accepted for inclusion in Graduate Theses & Non-Theses by an authorized administrator of Digital Commons @ Montana Tech. For more information, please contact sjuskiewicz@mtech.edu.

Using Unmanned Aircraft System (UAS)-borne high-resolution
hyperspectral imaging and gamma radiometry for rare earth element
exploration in the Bearpaw Mountains, Montana USA

by
Emma Kamp

A thesis submitted in partial fulfillment of the
requirements for the degree of

Geoscience, Geophysical Engineering Option, M.S.

Montana Tech

2024



Abstract

The radiometric signature of thorium, in combination with the hyperspectral signature of carbonate minerals, can be a useful indicator of rare earth mineral occurrences in air-borne geophysical exploration. Recent technological advancements have allowed unmanned aircraft system (UAS)--borne spectral imaging and gamma-ray spectroscopy systems to acquire high-spatial-resolution data. In this study, we attempted to define and map an area of interest for rare earth mineral exploration using UAS-borne spectral and gamma-ray spectroscopy systems. Gamma-ray spectroscopy data were used to define an area of interest. Short-wave infrared imagery was used to detect and map carbonate minerals within the area of interest. Gamma-ray spectroscopy data successfully outlined an area of interest for rare earth element exploration consistent with ground-truth rock samples, geochemical analysis, and previous geological mapping. Hyperspectral image classification using spectral angle mapper (SAM) and spectral information divergence-spectral angle mapper hybrid method (SID-SAM) methods mapped carbonate minerals within the defined area of interest most successfully. Combining high-resolution UAS remote sensing with geophysical methods provides more robust results than a single method alone.

Keywords: hyperspectral remote sensing; gamma-ray spectroscopy; rare earth minerals; Unmanned Aircraft System; geochemical analysis

Dedication

To my husband who encouraged me in my decision to go back to school, I could not have done this without you. Thank you for always supporting me.

Acknowledgments

This research was sponsored by the Combat Capabilities Development Command Army Research Laboratory and was accomplished under Cooperative Agreement Number W911NF-22-2-0015. The views and conclusions contained in this document are those of the authors, and should not be interpreted as representing the official policies, either expressed or implied, of the Combat Capabilities Development Command Army Research Laboratory or the U.S. Government. The U.S. Government is authorized to reproduce and distribute reprints for Government purposes notwithstanding any copyright notation herein.

Thank you to the Chippewa Cree Tribe for allowing me access to their land to conduct this research. I would like to thank Army Research Laboratory for providing the funding for this research. I would also like to thank Dr. Xiaobing Zhou for taking me in and his guidance throughout my time at Montana Tech. A big thank you to James Jonas for his UAS expertise and assistance in data collection and to Marisa Redgrave for her assistance both in and out of the field. To my committee members, Dr. Curtis Link, Dr. Christopher Gammons, and Gary Wyss, thank you for your guidance and expertise. This paper will be submitted for publication in the journal *Remote Sensing of Environment*.

Table of Contents

ABSTRACT	II
DEDICATION	III
ACKNOWLEDGEMENTS	ERROR! BOOKMARK NOT DEFINED.
LIST OF TABLES	VI
LIST OF FIGURES.....	VII
LIST OF EQUATIONS	IX
1. INTRODUCTION	1
2. STUDY AREA	5
2.1. <i>Vegetation</i>	7
3. MATERIALS AND METHODS	8
3.1. <i>Fieldwork</i>	8
3.2. <i>XRF, XRD, SEM</i>	9
3.3. <i>Endmembers for Hyperspectral Classification</i>	10
3.4. <i>Data Processing</i>	13
4. RESULTS.....	17
4.1. <i>XRF, XRD, SEM</i>	17
4.2. <i>Gamma-ray spectrometry</i>	19
4.3. <i>Hyperspectral Classification</i>	21
5. DISCUSSION	25
6. CONCLUSIONS.....	29
7. REFERENCES	31

List of Tables

Table 1: Mean, median, and standard deviation XRF concentration results (unit: ppm) from 11 carbonate material scans and nine altered shonkinite material scans taken at different spots on the samples. Both materials were collected from Trench 2. Results for Strontium (Sr), Thorium (Th), Iron (Fe), Barium (Ba), Cerium (Ce), Lanthanum (La), Niobium (Nb), and Yttrium (Y).....	17
---	----

List of Figures

- Figure 1: Maps of study area: (a) location of study area in Montana, (b) the approximate area of the Vermiculite Mine and Bower Peak Prospect (adapted from McNary (1981)), and (c) geology of the Bowery Peak prospects and surrounding area (adapted from Bergantino et al. (2002) and Pecora (1957)). The black box shows the approximate area of hyperspectral and gamma-ray data collection.....6
- Figure 2: Surface geologic map of Trench 2 in the Bowery Peak Prospect (adapted from McNary (1981) ‘Surface Geologic Map of Trench 2’).7
- Figure 3: Trench 2 (a) altered carbonate-rich and (b) altered shonkinite material. Dime shown for scale.....10
- Figure 4: Endmember spectra chosen for classification and grouped for clarity (a) carbonate, (b) rock type, (c) weathering, and (d) vegetation. Noisy and water bands were removed, and the spectra were resampled to the Co-Aligned SWIR spectral bands, shown in the second column.....12
- Figure 5: Spectra collected from a Trench 2 carbonate rock sample measured by the Evolution SR-5000 spectroradiometer show absorption features for Nd (579nm, 739 nm, 800nm, and 863 nm), parisite (1455 nm and 1550 nm), and carbonate (2339 nm).....13
- Figure 6: Simplified flow chart of data processing steps.....16
- Figure 7: The SEM-BSE images from the Trench 2 carbonate material sample. Brt – Barite, Str - strontianite, Qrz – quartz, Cal – calcite, Syn – synchysite, Par – parisite, Bas – bastnaesite.19

- Figure 8: Analyzed results from gamma-ray radiation: (a) 40-K concentrations (%), (b) 232-Th concentrations (ppm) with white contour line defining area of interest, and (c) 238-U concentrations (ppm).20
- Figure 9: Classified images overlain on the false color images from the hyperspectral images of 3-cm resolution. Panel (a) shows the classification results using the SAM method, panel (b) shows the results using the SID method, and panel (c) shows the results using the SID-SAM method. The white contour shows the 45 ppm 232-Th contour outlining an area of high probability for carbonate and REE minerals.....21
- Figure 10: Classified images overlain on the false color images from the hyperspectral images of 5-cm resolution. Panel (a) shows the classification results using the SAM method, panel (b) shows the results using the SID method, and panel (c) shows the results using the SID-SAM method. The white contour shows the 45 ppm 232-Th contour outlining an area of high probability for carbonate and REE minerals.....22
- Figure 11: Classification results of Trench 2 of the 3-cm dataset using (a) the SAM, (b) the SID, and (c) the SID-SAM methods.24
- Figure 12: Classification results of Trench 2 of the 5-cm dataset using (a) the SAM, (b) the SID, and (c) the SID-SAM methods.25

List of Equations

(Equation 1)	14
(Equation 2)	14
(Equation 3)	14

1. Introduction

Rare earth elements (REEs) have become vital to modern life due to their application in computers and smartphones, green energy technologies - especially wind turbines (permanent magnets), electric vehicles, and defense technologies (Van Gosen et al., 2014; Golroudbary et al., 2022). In recent years, 85-95 percent of the world's REEs have been provided by China, leading to a worldwide increase in exploration for economic deposits of REEs (Van Gosen et al., 2014). Carbonatites of alkaline-carbonate complexes are a main exploration target for REEs and critical minerals. Exploration for these deposits have primarily used traditional prospecting and geological methods, which can be time-consuming and expensive, and the spatial distribution of geochemical analysis is limited. Carbonatites, defined as an igneous rock containing more than 50% modal primary carbonate (Le Maitre, 2002), lend themselves to remote sensing approaches because they often contain spectrally active minerals and trace amounts of radioactive materials that can be detected with hyperspectral and gamma-ray spectroscopy methods (Simandl & Paradis, 2018).

Radiometric surveys provide spatial information about radioactive isotopes of potassium (K), thorium (Th), and uranium (U) concentrations, typically associated with carbonatites and REE-bearing minerals such as monazite, synchysite, and bastnaesite (Simandl & Paradis, 2018; Shives, 2015). A ground-based radiometric survey was used while investigating the carbonatites of the Rocky Boy Stock in the Bearpaw Mountains to help geologists define the extent of the radioactive zone related to the carbonatite intrusion and detect other areas containing radioactive minerals (McNary, 1981). The advent of airborne radiometric surveys provided a tool to explore more areas and terrain inaccessible to traditional geological methods. Shives (2015) and Simandl and Paradis (2018) explored several examples where radiometric surveys were helpful in

delineating carbonatites and their mineralized units by identifying variations in detected K, Th, and U.

Field spectrometry data and airborne hyperspectral imaging are other geophysical methods that have been useful in identifying and mapping the mineralogy of carbonatite complexes (Neave et al., 2016; Rowan et al., 1995). Spectrometers and hyperspectral sensors collect information across the electromagnetic spectrum to create a spectral signature for a material or a pixel. This is useful because all materials have a unique spectral signature. REEs, specifically neodymium, and carbonate minerals have distinct absorption features in the visible-near infrared (VNIR, 400 – 1,000 nm) and shortwave infrared (SWIR, 1,000 – 2,500 nm) region of the electromagnetic spectrum that can be used to detect carbonatites and REE mineralization (Neave et al., 2016; Rowan et al., 1986; Boesche et al., 2015).

Using point spectroscopy methods, neodymium (Nd) shows characteristic narrow absorption features in the VNIR region centered around 580nm, 740nm, 800nm, and 870nm (Neave et al., 2016; Rowan et al., 1986; Boesche et al., 2015). Detecting these narrow absorption features with hyperspectral imaging requires high spectral and spatial resolution and signal-to-noise ratio (Booyesen et al., 2019, 2020; Herrmann, 2015). REE-bearing carbonates often occur in small geological structures, less than one meter to ten meters thick, such as dikes and plugs (Pecora, 1956).

Current airborne and satellite hyperspectral imaging systems such as Airborne Visible InfraRed Imaging Spectrometer (AVIRIS), Hyperion, HyMap, and EnMap collect hyperspectral data at meter to tens of meter pixel resolution. Data collected at meter to ten-meter spatial resolution do not have the spatial resolution and signal-to-noise ratio to map Nd reliably in small (less than ten-meter) geologic structures (Neave et al., 2016; Boesche et al., 2015; Herrmann,

2015). Nd absorption features may get lost in larger pixel sizes because of spectral mixing and masking. Since hyperspectral imaging only detects superficially, the spectrum from iron oxide staining and lichen can mask or mix with the spectral signatures of rocks (Herrmann, 2015; Rautiainen et al., 2024; Rollin et al., 1994).

The carbonate feature in the SWIR region has also been used as a more general remote-sensing indicator for carbonatites associated with rare earth element mineralization (Rowan et al., 1995). Airborne and satellite hyperspectral SWIR data have proved beneficial in outlining carbonatite complexes (Bedini & Rasmussen, 2018; Booysen et al., 2019). Until recently, the SWIR region of hyperspectral imagery has been limited to airborne or satellite imagery in the scale of meters to tens of meters spatial resolution. Studies using airborne and satellite SWIR imagery have been limited to areas with sparse vegetation cover because of spectral mixing at those spatial resolutions. As REE-bearing carbonates often occur in small geologic structures, increasing spatial resolution is one approach to overcome spectral mixing caused by vegetation and weathering to improve the mapping of small geologic structures.

UAS-borne hyperspectral imaging has become a valuable technique for obtaining high-resolution data, in the centimeter scale, for research in agriculture (Vanegas et al., 2018), forestry (Sandino et al., 2018), mining (Barton et al., 2021), and exploration (Booyesen et al., 2019, 2020; Jackisch et al., 2020). The method has been used in several studies to explore carbonatites and rare earth minerals (Booyesen et al., 2019, 2020; Jackisch et al., 2020), but data have been limited to the VNIR spectral region, and detection of Nd has been limited by sensor signal-to-noise (SN) ratio and REE grades. Recent technological advancements have allowed UAS-borne spectral sensors in the SWIR region to detect and map carbonate, clay, phyllosilicates, and sulfate minerals (Barton et al., 2021).

Techniques combining multi-scale hyperspectral imaging and airborne geophysical methods, such as gamma radiometry and magnetic surveys, have been employed to improve the robustness of geologic mapping results (Bedini & Rasmussen, 2018; Jackisch et al., 2020). The work presented here is a pioneering study of UAS-based high-resolution hyperspectral imagery in the SWIR region, lidar, and gamma-ray spectrometry data for mapping and identifying areas of interest for rare earth mineral exploration. The primary goals of the study were to determine whether high-resolution hyperspectral imagery could reliably map the distribution of carbonate minerals in outcrops and trenches in a weathered and thinly vegetated environment and if this mapping can add to gamma mapping of an area to improve the delineation of areas of interest for rare earth mineral exploration. Geochemical analysis using scanning electron microscope energy dispersive X-ray spectroscopy (SEM-EDS), X-ray diffraction (XRD), and X-ray fluorescence (XRF) were used to evaluate rare earth minerals and critical materials from hand samples in the study area. Secondly, two hyperspectral scans of the study area were collected at different elevations above ground level to examine the potential impact of differences in spatial resolution on UAS-based mineral exploration.

2. Study Area

The Bearpaw Mountains, located in north-central Montana (Figure 1(a)), formed in the middle of the Eocene. They are a part of the Central Montana Alkaline Province. The Rocky Boy Stock is the most extensive and complex stock in the Bearpaw Mountains, covering about 12 square miles. Most of the stock comprises pyroxenites, shonkinites and syenites, nepheline or pseudoleucite shonkinites and syenites, monzonites, and pegmatite-bearing nepheline syenites (Pecora, 1942).

The Bearpaw Mountains have been the focus of geologic mapping since the 1890's. Major exploration of the mineral resources in the Rocky Boy stock of the Bearpaw Mountains began in the early 1930's and continued into the 1990's. The research during this time focused on mapping the geology of the Rocky Boy stock and commodity exploration, including natural gas, coal, and uranium (McNary, 1981). During this time, several rare-earth-bearing carbonates were identified, primarily in the carbonatite-pegmatite dikes of the Vermiculite Mine Prospects

of the Rocky Boy Stock (McNary, 1981; Pecora, 1962) (Figure 1(c)).

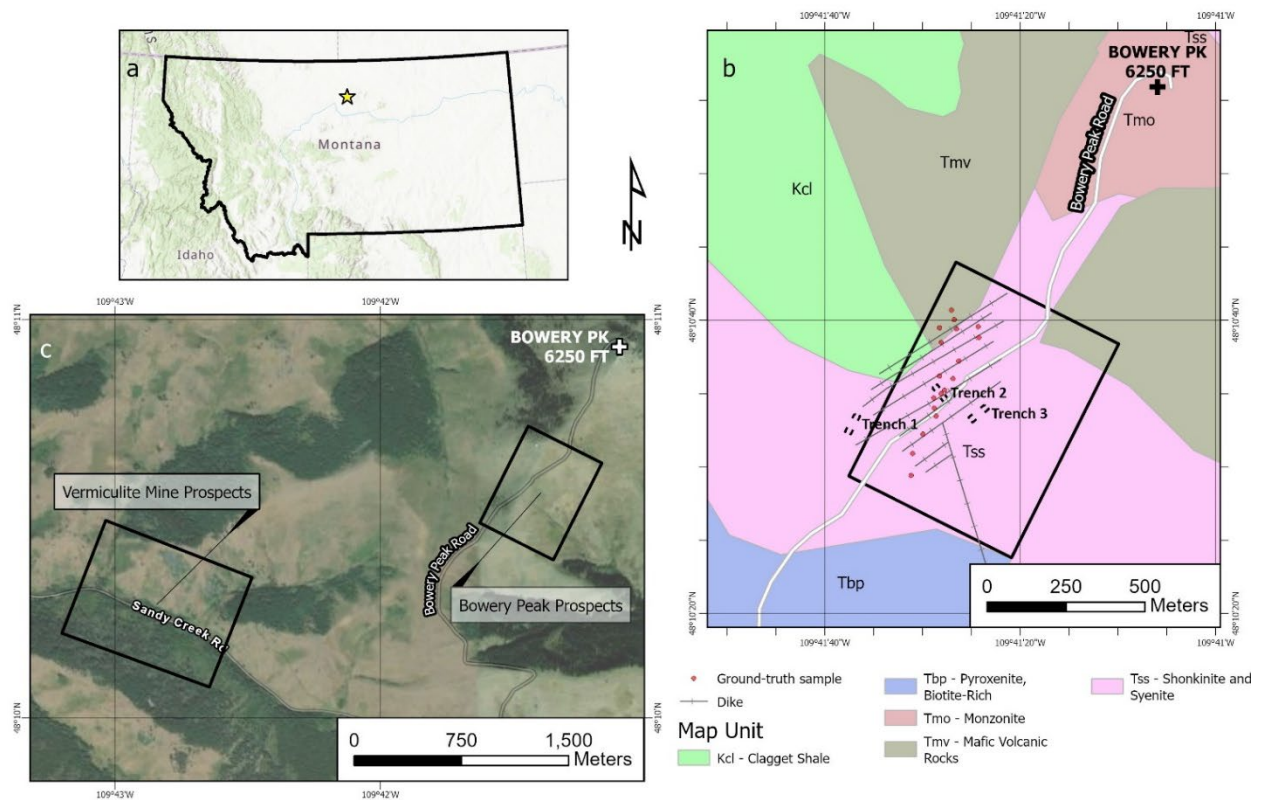


Figure 1: Maps of study area: (a) location of study area in Montana, (b) the approximate area of the Vermiculite Mine and Bower Peak Prospect (adapted from McNary (1981)), and (c) geology of the Bower Peak prospects and surrounding area (adapted from Bergantino et al. (2002) and Pecora (1957)). The black box shows the approximate area of hyperspectral and gamma-ray data collection.

The U.S. Bureau of Mines used soil samples, rock samples, and scintillometer readings to determine the extent of the carbonate-pegmatite dikes, identifying another area of alteration and carbonate rock named the Bower Peak prospects. The Bower Peak prospects are a 400 ft by 600 ft (122 m by 183 m) area with three dozer-cut trenches (Trench 1, 2, and 3) (Figure 1(b)). Shonkinite country rock is cut by porphyritic syenite, aegerite, and latite dikes trending northeast. The best outcropping of alteration and carbonate material occurs in Trench 2 (Figure 2), where weathered shonkinite blocks are found in a matrix of gray-to-white carbonate-rich

material and red-brown oxidized material thought to be altered shonkinite (McNary, 1981). Carbonate-rich and altered shonkinite float were also found in Trench 3 (McNary, 1981).

The soil samples collected from the Bowery Peak prospects during the field investigations in 1978 and 1979 suggest elevated uranium southeast of Trench 2 (McNary, 1981). The carbonate-rich veins and alteration material within Trench 2 were never formally defined as carbonatite. However, scintillometer readings collected using a Geometrics gamma-ray spectrometer, and soil/rock sample analysis indicated elevated thorium and rare earth element levels within the alteration zone (McNary, 1981). Aside from the work by the U.S. Bureau of Mines, no further exploration of the Bowery Peak prospects has been conducted.

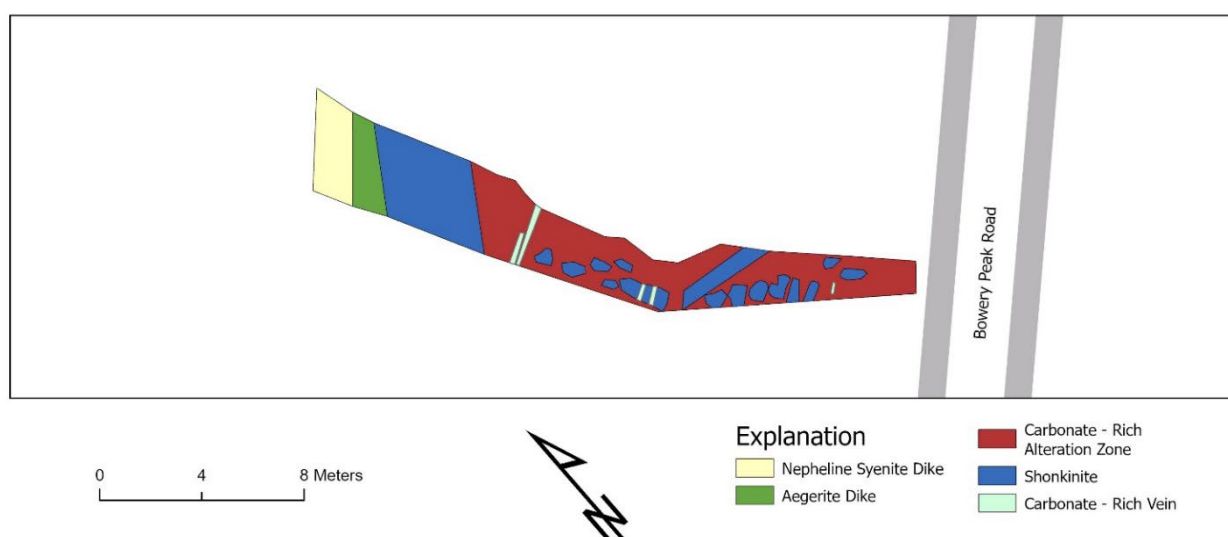


Figure 2: Surface geologic map of Trench 2 in the Bowery Peak Prospect (adapted from McNary (1981) 'Surface Geologic Map of Trench 2').

2.1. Vegetation

The Bowery Peak prospects were chosen due to their lack of tree cover compared to the Vermiculite Mine prospect. From the air, the view of the Bowery Peak prospects are not impeded by trees. The area outside the outcrops and trenches was covered by dry grass and occasionally by shrubs. Most outcrops in the area were weathered and covered in lichen. Lichen

is spectrally active in the SWIR range, which could impact the results of hyperspectral mapping (Rautiainen et al., 2024; Rollin et al., 1994).

3. Materials and Methods

3.1. Fieldwork

Hyperspectral imagery and gamma data were collected on October 8, 2023.

Hyperspectral imaging was carried out with the Headwall Photonics Co-Aligned HP (400 – 2500nm) hyperspectral imaging plus lidar system. The sensor contains Headwall Photonics co-aligned VNIR and SWIR systems, an integrated high-performance global positioning system/inertial measurement unit (GPS/IMU) system, and an integrated Velodyne Light Detection and Ranging (LiDAR) system. The SWIR system covers 900-2500 nm with 270 spectral bands, and the VNIR system covers 400-1000 nm with 273 spectral bands. The co-aligned system was hard-mounted to a Freefly AltaX drone. Two hyperspectral flights were flown midday between 11 am and 3 pm. The first flight was flown at an average height above ground of 80 m for an approximate spatial resolution of 5 cm. The data collected from this flight are referred to as the 5-cm dataset. The second hyperspectral flight flew at an average height above ground of 60 m for an approximate spatial resolution of 3 cm. The data from this flight are referred to as the 3cm dataset. Both VNIR and SWIR data were collected for the 3- and 5-cm datasets. Evaluation of the VNIR data in both datasets indicated that the signal-to-noise ratio was too low to reliably classify pixels containing neodymium using the methods presented in this paper. Due to this, only results for the classification of SWIR data will be displayed and discussed.

Gamma data were collected after the hyperspectral scans using the Medusa MS-1000 sensor. The sensor was mounted on a FreeFly AltaX drone. The average height above ground

was 80 m, the flight speed was set to 5 m/s, and the sampling frequency was 1hz, so that the sampling interval was approximately 5 m. The sensor was factory set for online radionuclide analysis of 40-K, 238-U, 232-Th, and 137-Cs.

Ground truth samples were collected during the field campaigns of September 1-2 and September 22-23 from Trench 2 and outcrops in the surrounding area. Samples of each rock type were collected and scanned using a Spectral Evolution SR-5000 Spectroradiometer in the laboratory at Montana Tech, including scans of weathered, lichen, and fresh surfaces. The Spectral Evolution SR-5000 spectra were imported into The Spectral Geologist (TSG) software for classification and the ground truth library selection.

3.2. XRF, XRD, SEM

XRF scans were used to estimate the concentration of rare earth elements lanthanum (La) and cerium (Ce) in rock samples collected from Trench 2. Other measurements of interest were concentrations of iron (Fe), strontium (Sr), thorium (Th), and barium (Ba), which demonstrate compositional differences between the altered carbonate-rich (Figure 3(a)) and altered shonkinite (Figure 3(b)) Trench 2 samples. Concentrations of critical elements niobium (Nb) and yttrium (Y) were also evaluated.

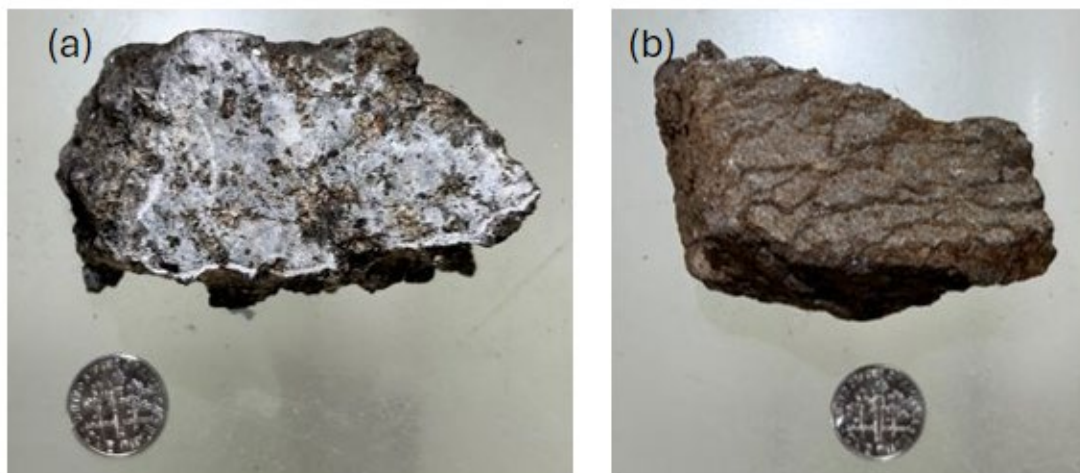


Figure 3: Trench 2 (a) altered carbonate-rich and (b) altered shonkinite material. Dime shown for scale.

XRD analysis was used for rock identification and mineral analysis of hand samples collected in the field. Trench 2 samples were chosen based on color and XRF results. Ground-truth samples were chosen to be representative of the country rock, dikes, and altered material in the study area based on appearance and relative abundance of mafic to felsic minerals from hand sample analysis.

One altered carbonate-rich sample collected from Trench 2 was chosen for further SEM analysis using TESCAN MIRA3. The work included SEM backscatter electron imagery (BSE) and SEM-EDS spot analysis.

3.3. Endmembers for Hyperspectral Classification

Figure 4 shows the primary spectral reflectance classes chosen based on Spectral Evolution SR-5000 spectra and XRF, XRD, and SEM-EDS results. The second column shows the spectrum reduced to the same bands as the co-aligned imaging system in SWIR spectral range as they were used in SWIR imagery classification. The spectral classes display absorption features in the SWIR region due to cellulose (lichen) (Rautiainen, 2024), CO_3^{2-} radical (carbonate) (Rowan et al., 1986), and Mg-OH bonding (phlogopite) (Peyghambari & Zhang,

2021), as well as dispersed absorption in the VNIR range from Fe^{3+} (goethite) (Peyghambari & Zhang, 2021), Fe^{2+} (nepheline syenite/pyroxene +phlogopite), and transition series cations (pyroxene/aegirine) (Cloutis, 2002) which change the overall shape of the spectrum. Note that the rock-type spectrum demonstrates few absorption features after removing noisy, VNIR, and water bands, which may limit hyperspectral classification ability.

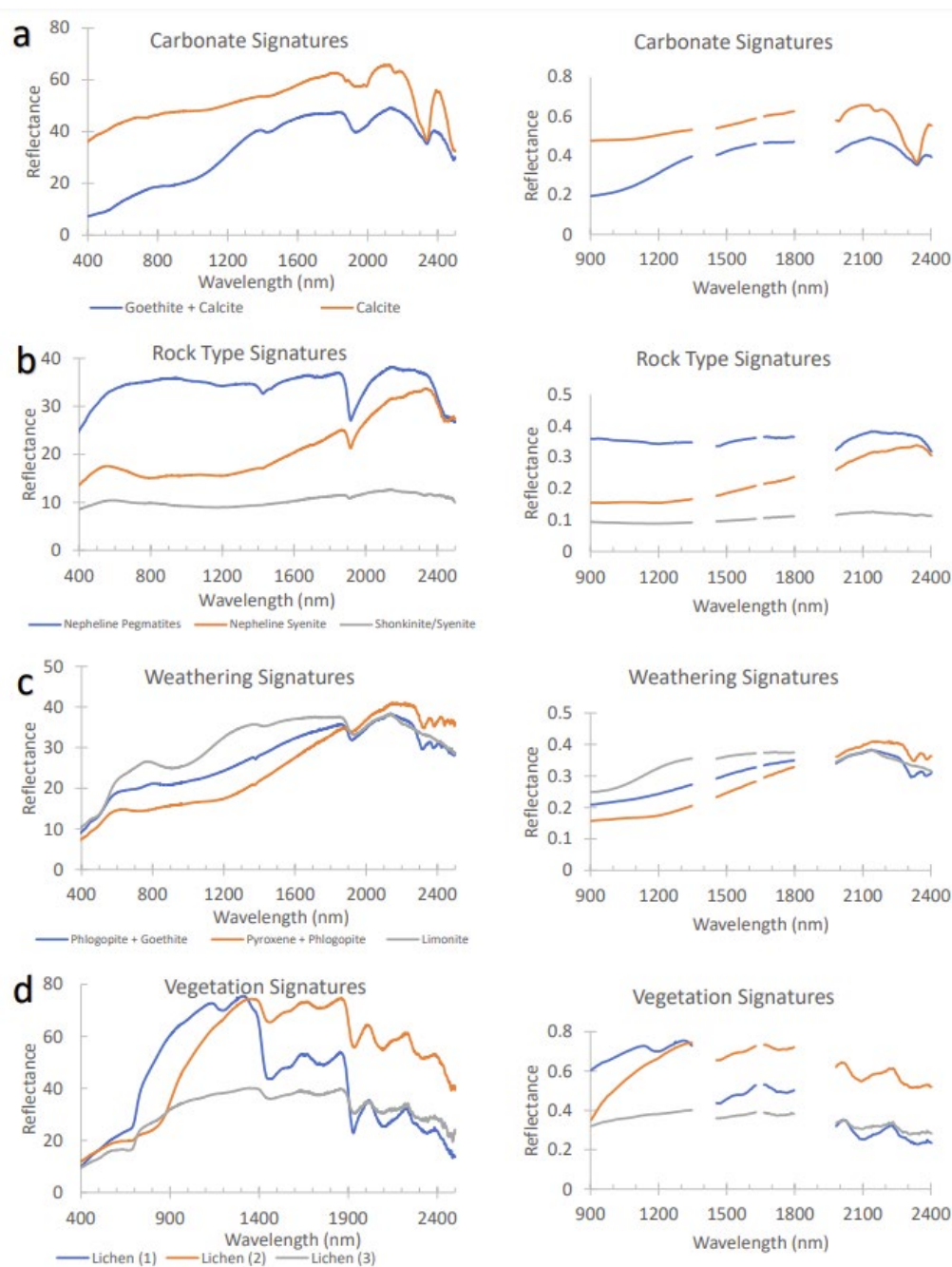


Figure 4: Endmember spectra chosen for classification and grouped for clarity (a) carbonate, (b) rock type, (c) weathering, and (d) vegetation. Noisy and water bands were removed, and the spectra were resampled to the Co-Aligned SWIR spectral bands, shown in the second column.

As shown in Figure 5, the spectra collected using the Spectral Evolution SR-5000 spectroradiometer of an altered carbonate-rich rock sample from Trench 2 display parisiite (Herrmann, 2015) and neodymium (Nd) (Rowan et al., 1986; Herrmann, 2015) absorption

features at 579 nm, 739 nm, 800 nm, 863 nm, 1455 nm, and 1550 nm. Despite the Spectral Evolution SR-5000 spectra results, absorption features that could be unequivocally assigned to REE were not noticed in the VNIR imagery pixels collected in the 3 cm or 5 cm datasets.

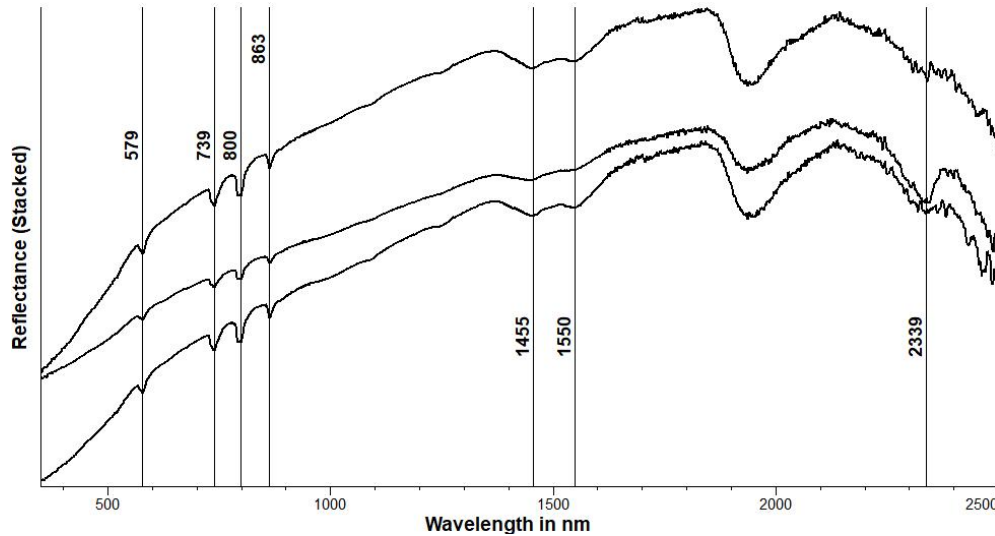


Figure 5: Spectra collected from a Trench 2 carbonate rock sample measured by the Evolution SR-5000 spectroradiometer show absorption features for Nd (579nm, 739 nm, 800nm, and 863 nm), parisite (1455 nm and 1550 nm), and carbonate (2339 nm).

3.4. Data Processing

The UAS-borne hyperspectral images collected by the co-aligned Hyperspectral imaging plus lidar system were reduced using Headwall Photonics Batch Processing Widget - SpectralView and MATLAB Image Processing Toolbox – Hyperspectral Imaging Library. A simplified flow chart of data processing steps is shown in Figure 6. Raw scan data were converted to spectral reflectance using SpectralView, using dark currents collected before scanning and scene white reference captured from a white reference panel placed in the scene. Spectral reflectance data were orthorectified using GPS data of the drone locations and a DEM created from LiDAR point cloud. Orthorectified images were then stitched into a multi-orthorectified image using SpectralView. The SpectralView orthorectification process adjusts to a uniform scale, removing effects due to lens distortion, topography, and spectrometer angle

variation. Image pre-processing is necessary before image classification. Firstly, water bands at 1346-1454 nm and 1796-1982 nm for each pixel were removed to enhance signal-to-noise ratio. Secondly, bands from 1628-1664 nm and > 2400 nm that have too much sensor noise were also removed. Thirdly, SWIR data were filtered using a Savitzky-Golay polynomial filter of order 3, and a moving window of size 100.

The pre-processed image was then classified using the MATLAB Image Processing Toolbox—Hyperspectral Imaging Library. Three classification methods were used: spectral angle mapper (SAM), spectral information divergence (SID), and spectral information divergence-spectral angle mapper hybrid method (SID-SAM). Reference spectra were taken from the ground-truth samples using the Spectral Evolution SR-5000 spectroradiometer defined in section 3.3.

The SAM algorithm (Equation 1) has been widely used in hyperspectral image analysis for mineral identification (Barton et al., 2021). The SAM method measures the similarity between the test spectrum at each pixel of an image to be classified and the library of reference spectra of target rocks or minerals (Kruse et al., 1993). The test spectrum (t) and a reference spectrum (r) are treated as vectors with as many dimensions (n) as the number of hyperspectral bands. The SAM algorithm computes the similarity or spectral angle ($< 180^\circ$) between the two vectors by taking the inverse cosine of the dot product of the two spectra in the n -space:

$$a = \cos^{-1}\left(\frac{\sum_{i=1}^n t_i r_i}{\sqrt{\sum_{i=1}^n t_i^2} \sqrt{\sum_{i=1}^n r_i^2}}\right) \quad (1)$$

The smaller the spectral angle (a) is, the stronger the match between the reference and test spectra will be. For a test spectrum to be considered a match to a reference spectrum, the spectral angle must fall within a user-defined threshold. The lower the threshold value is, the

more similar the two spectra are, and fewer pixels in the image will be classified as the class of the reference spectrum. The SAM method has been shown to have advantages in identifying rocks and minerals with low albedo and flat spectral features, considering the overall shape of spectra rather than specific absorption features (Chen et al., 2010). The SAM method faces challenges with spectral mixing in medium-resolution images (Kale et al., 2017).

The SID algorithm is not as widely used in hyperspectral image analysis, but SID-based lithological mapping has generated lithological maps comparable to those of the SAM algorithm (Rao & Guha, 2016). SID is a probabilistic method that calculates the statistical divergence to derive the similarity between the reference and test spectra (Equation 2) (Chang, 2000). Assuming r and t are vectors of reference and test spectra, respectively, SID is calculated as follows:

$$SID = \sum_{i=1}^n t_i \log\left(\frac{t_i}{r_i}\right) + \sum_{i=1}^n r_i \log\left(\frac{t_i}{r_i}\right). \quad (2)$$

As with the SAM method, for a pixel spectrum (test spectrum) to be considered a match to a reference spectrum, the SID score must fall within a user-defined threshold value, with smaller SID scores indicating a more robust match.

The SID-SAM method (Equation 3) combines the SAM and SID approaches, where a is the angle calculated by the SAM algorithm (Chang, 2004), and SIDSAM is calculated as follows:

$$SIDSAM = SID \times \tan(a). \quad (3)$$

This method can increase spectral discriminability by making the similarity or dissimilarity of two spectra more distinct (Du et al., 2004).

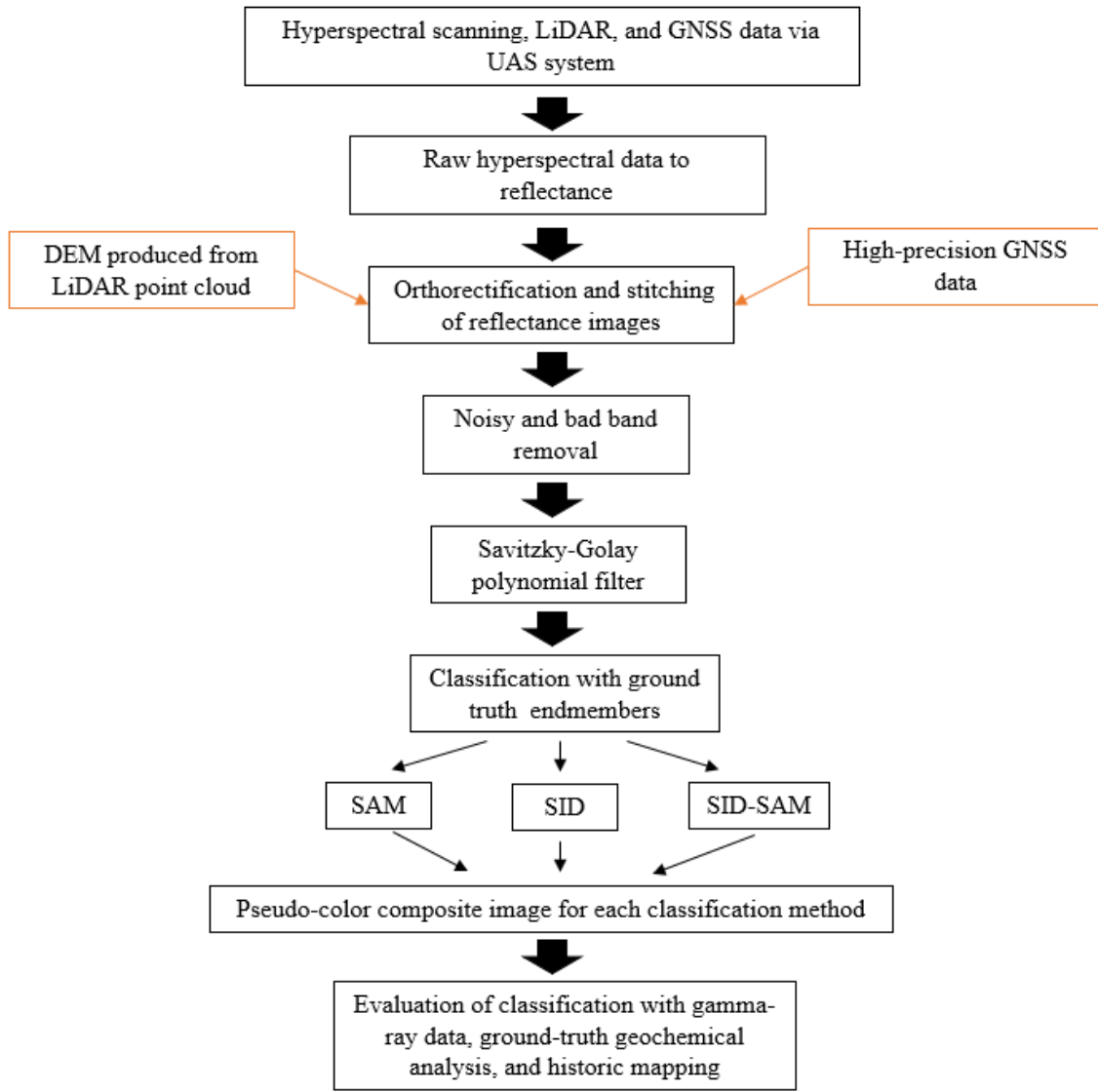


Figure 6: Simplified flow chart of data processing steps.

Radionuclide data collected from the Medusa MS-1000 sensor was converted to concentration in ^{238}U (ppm), ^{232}Th (ppm), and ^{40}K (%). Estimated concentration data was imported to Oasis Montaj for gridding minimum curvature method to produce three heat maps representing estimated concentrations of ^{238}U , ^{232}Th , and ^{40}K .

4. Results

4.1. XRF, XRD, SEM

Table 1 shows the XRF results of Trench 2 samples, displaying the compositional differences between the carbonate and altered shonkinite materials. The XRF detected higher La, Ce, Th, Sr, and Ba concentrations in the Trench 2 carbonate material. The XRF detected lower La, Ce, Sr, Th, and Ba concentrations and higher Fe concentrations in the altered shonkinite material.

Table 1: Mean, median, and standard deviation XRF concentration results (unit: ppm) from 11 carbonate material scans and nine altered shonkinite material scans taken at different spots on the samples. Both materials were collected from Trench 2. Results for Strontium (Sr), Thorium (Th), Iron (Fe), Barium (Ba), Cerium (Ce), Lanthanum (La), Niobium (Nb), and Yttrium (Y).

	Carbonate Material				Altered Shonkinite Material			
	Mean	Median	Std DevS	Std DevP	Mean	Median	Std DevS	Std DevP
Sr	2,360	2,320	314	299	524	461	265	250
Th	1,030	972	502	458	81	86	32	30
Fe	13,900	9,220	11,600	11,100	64,100	65,300	18,400	17,400
Ce	4,790	3,720	2,780	2,650	628	636	332	313
La	2,990	2,470	1,660	1,580	393	437	206	194
Ba	20,900	16,800	11,100	10,600	3,350	3,220	2,435	2,300
Nb	54	43	34	32	124	112	43	41
Y	321	306	152	145	153	107	97	92

The XRD results of the two Trench 2 materials showed that the white-gray carbonate material was primarily composed of calcite, and the red-brown oxidized material was composed of orthoclase and phlogopite. XRD results for remaining ground-truth samples indicated the appropriate mineral composition for mafic nepheline syenite, syenite, porphyritic nepheline syenite, and shonkinite based on the classification described by Bergantino et al. (2002).

The results of XRD analysis and description of rock classes align well with previous investigations of the Rocky Boy Stock and the geology of alkalic-carbonatite complexes (Pecora,

1957, 1956, 1942; Bergantino et al., 2002; McNary, 1981). As noted in Section 3.3, endmember rock classes were reduced to shonkinite/syenite, nepheline syenite, and nepheline porphyry. The decision to reduce endmember rock classes was motivated by the similarity in spectral shape and spectral absorption features between syenite, shonkinite, and mafic nepheline syenite.

Figure 7 shows a sample of the SEM imagery. The SEM-EDS results of the altered carbonate-rich material from Trench 2 indicate the presence of carbonate minerals with rare earth elements: synchysite—(Ce), bastnaesite—(Ce), and parisite—(Ce). Other carbonate minerals include calcite and strontianite. The presence of strontianite explains the XRF results showing elevated Sr. Quartz and barite were also identified. Trace amounts of thorium were also detected with the rare earth carbonate minerals.

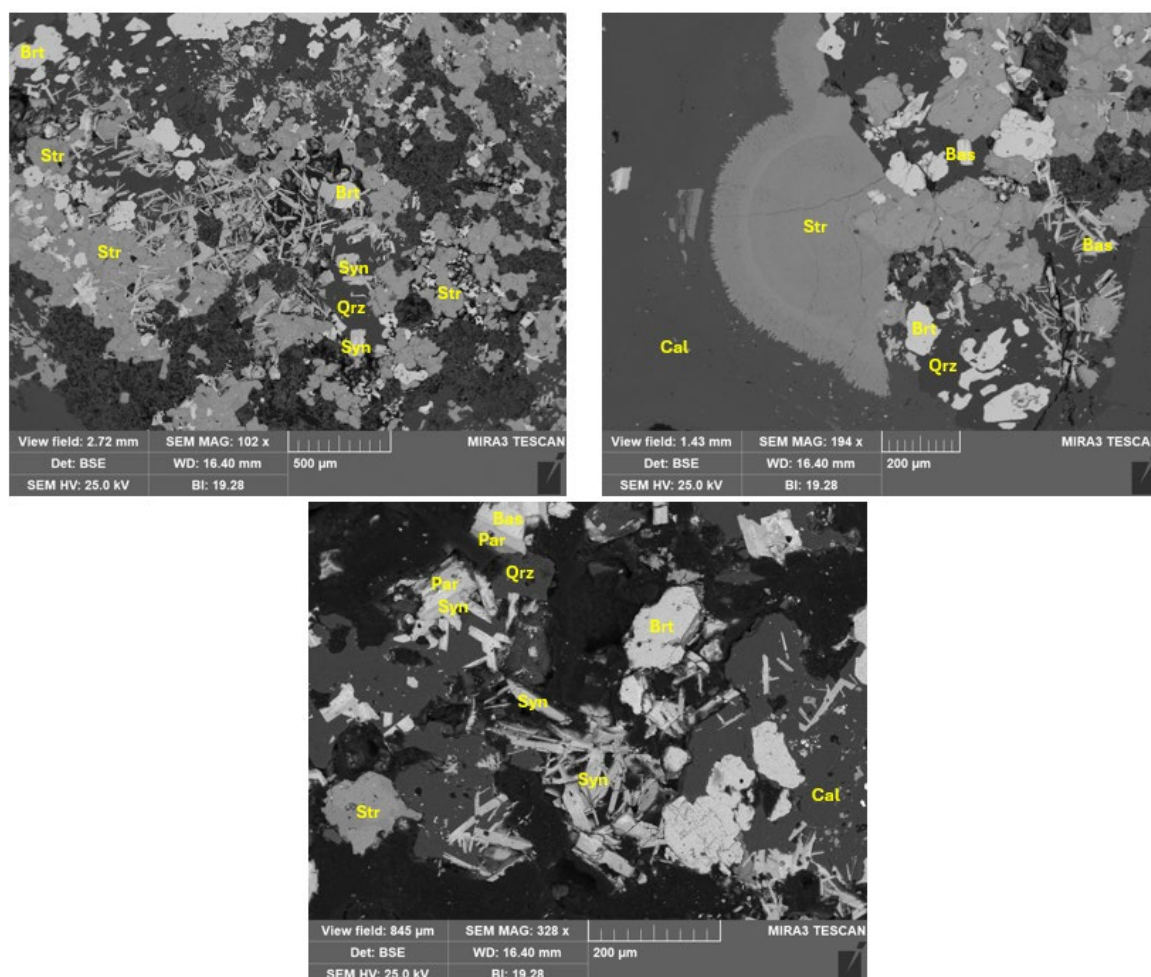


Figure 7: The SEM-BSE images from the Trench 2 carbonate material sample. Brt – Barite, Str - strontianite, Qrz – quartz, Cal – calcite, Syn – synchysite, Par – parisite, Bas – bastnaesite.

4.2. Gamma-ray spectrometry

Figures 8(a-c) show the distribution of ^{40}K , ^{232}Th , and ^{238}U , respectively, from the hyperspectral (1024 bands) gamma-ray radiation measurements. The gamma-ray spectrometry results indicate increased radioactive material surrounding Trench 2 and Trench 3 - the results of ^{40}K radionuclides (Figure 8(a)) display dispersed concentrations of radioactivity throughout the study area. The concentration map for ^{232}Th (Figure 8(b)) demonstrates a consolidated area of intense radiation covering both Trench 2 and Trench 3 and a secondary area southeast of the trenches. The white line is a contour line for 45 ppm that was used with hyperspectral

classification results to create an area of interest for high probability for carbonate and REE minerals. The concentration map for ^{238}U (Figure 8(c)), indicates a dispersed area of increased radiation around Trench 2, Trench 3, and the area southeast of the two trenches. Results of the uranium and thorium maps correlate well with analysis results from scintillometer, rock, and soil results at Bowery Peak by McNary (1981).

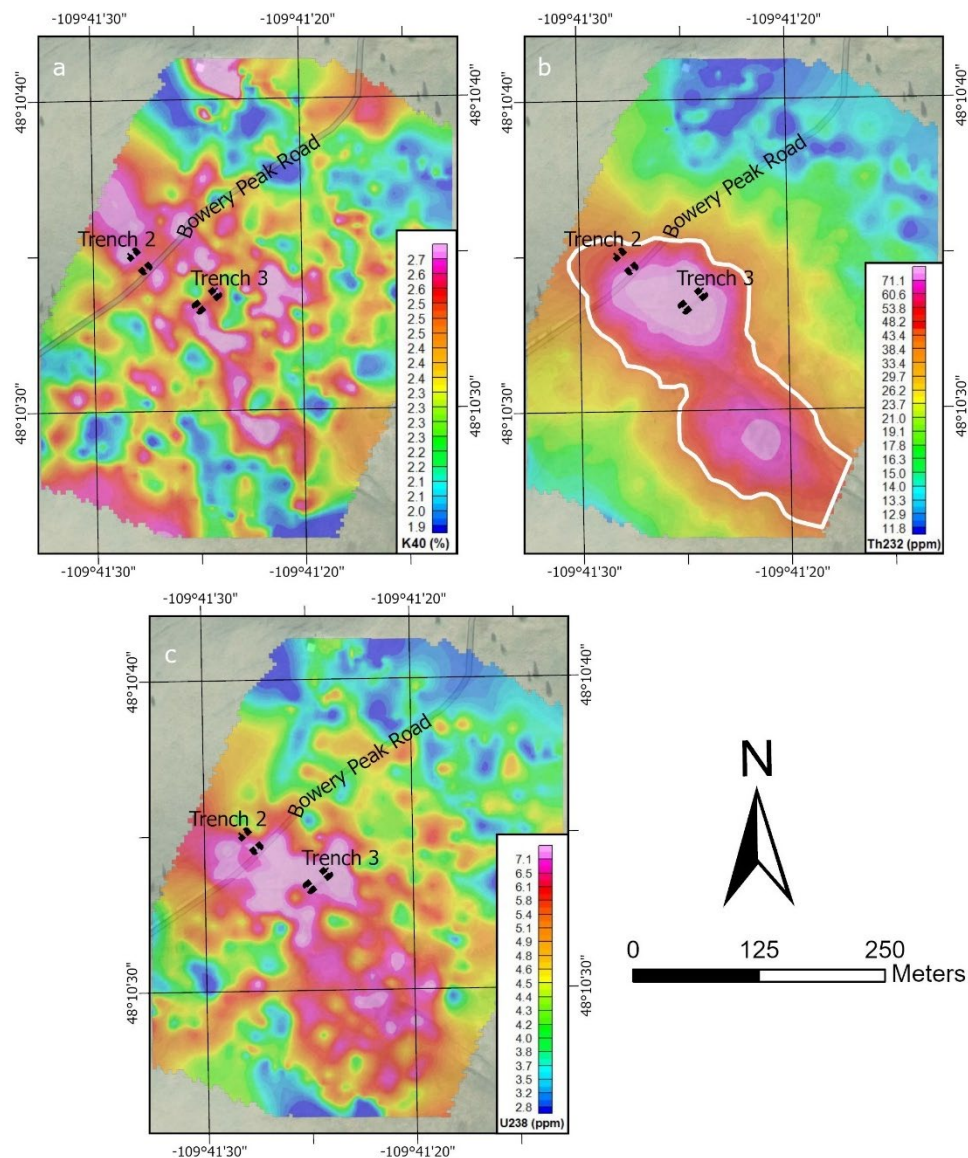


Figure 8: Analyzed results from gamma-ray radiation: (a) ^{40}K concentrations (%), (b) ^{232}Th concentrations (ppm) with white contour line defining area of interest, and (c) ^{238}U concentrations (ppm).

4.3. Hyperspectral Classification

The SWIR images with 3-cm and 5-cm resolutions collected using the co-aligned hyperspectral imaging and lidar system were classified using the endmembers described in Section 3.3 and classification methods in Section 3.4.

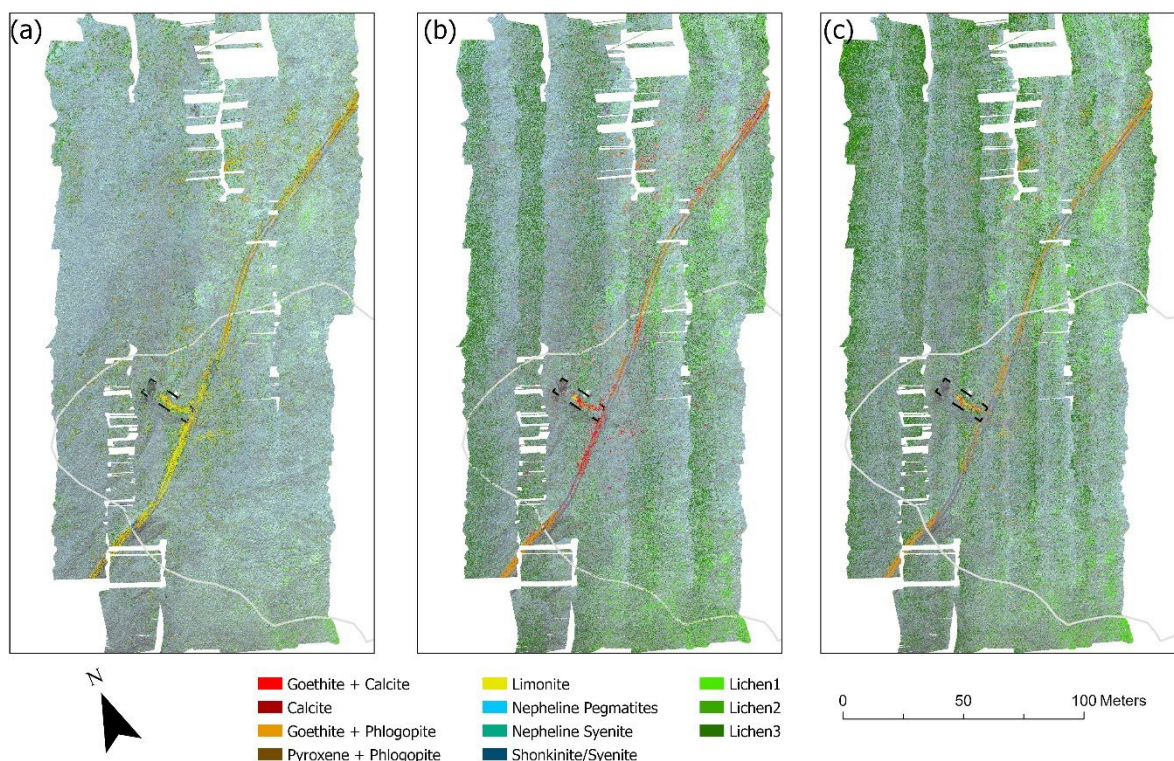


Figure 9: Classified images overlain on the false color images from the hyperspectral images of 3-cm resolution. Panel (a) shows the classification results using the SAM method, panel (b) shows the results using the SID method, and panel (c) shows the results using the SID-SAM method. The white contour shows the 45 ppm ^{232}Th contour outlining an area of high probability for carbonate and REE minerals.

Figure 9(a-c) and figure 10(a-c) show the classification results of the 3cm and 5cm datasets using the SAM, SID, and SID-SAM algorithms. Classification results of 3-cm and 5-cm datasets are similar, the 5-cm imagery covered more area and includes results over Trench 3. Figure 9(a) and 10(a) shows the results of the SAM algorithm, in both datasets, carbonate distribution is primarily within Trench 2. The SAM algorithm also primarily identified the

outcrops north of Trench 2 and 3 as goethite+phlogopite or limonite. Results of SID-SAM algorithm (Figure 9(c) and Figure 10(c)) identify more carbonate pixels but are consistent with the SAM algorithm and limit the distribution of carbonate within the Th outline, primarily within Trench 2. All three methods identify carbonate within Trench 3 from the 5-cm dataset which is likely the altered carbonate-rich float discussed in Section 2. Result of the SID algorithm (Figure 9(b) and 9(c)) show the greatest distribution of carbonate and are not limited to the Th outline, these results are not consistent with the other two methods, gamma-ray results, ground truth sample collection, or historical mapping and indicate an over classification of carbonate.

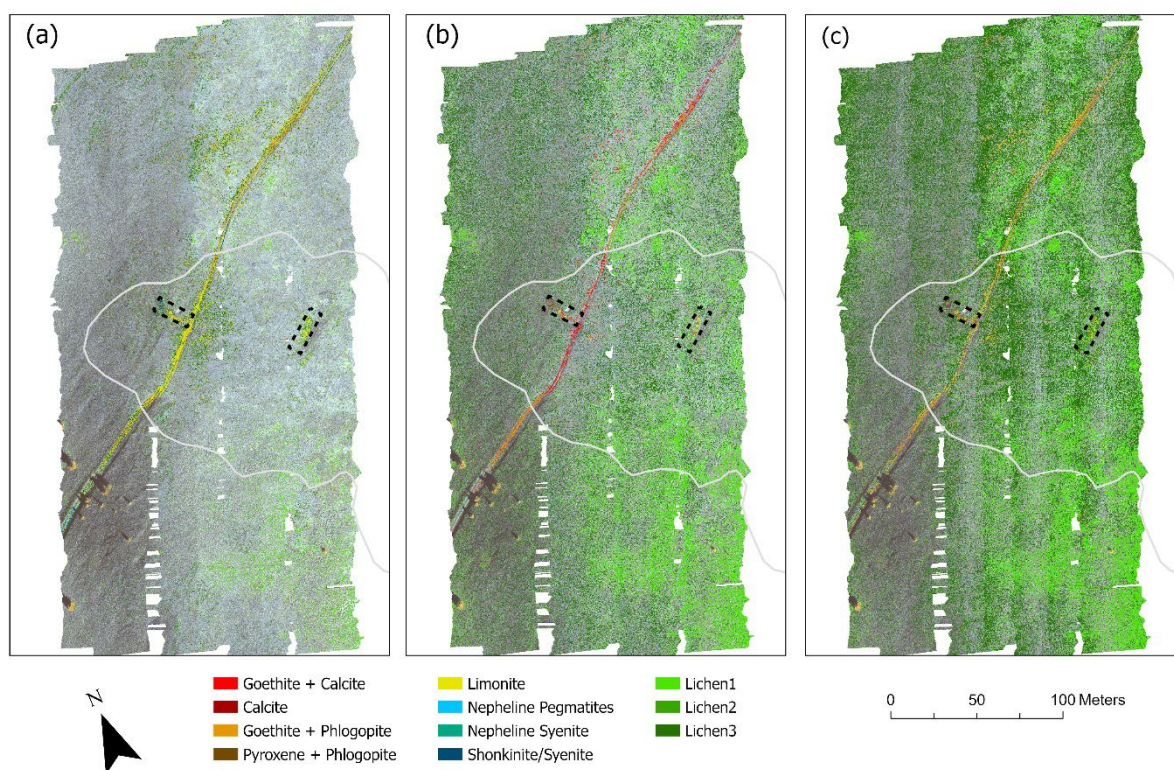


Figure 10: Classified images overlain on the false color images from the hyperspectral images of 5-cm resolution. Panel (a) shows the classification results using the SAM method, panel (b) shows the results using the SID method, and panel (c) shows the results using the SID-SAM method. The white contour shows the 45 ppm ^{232}Th contour outlining an area of high probability for carbonate and REE minerals.

Trench 2 has been identified as the prospect with best alteration, carbonate mineralization, and rare earth element enrichment. Figure 11(a-c) and Figure 12(a-c) show the

classification results over Trench 2 from the 3-cm and 5-cm datasets using the SAM, SID, and SID-SAM algorithms at a similar scale to Figure 2 for comparison. The SAM algorithm (Figure 11(a) and Figure 12(a)) has the greatest distribution of classified pixels between the three methods. The SAM algorithm was the most successful at identifying shonkinite/aegirine and nepheline syenite at the northwest edge of the trench, consistent with the historic surface geologic map (Figure 2). Results from the SAM and SID-SAM algorithms (Figure 11(a,c) and Figure 12(a,c)) show three primary locations of carbonate distribution consistent with the carbonate-rich veins mapped in the historic surface geologic map (Figure 2).

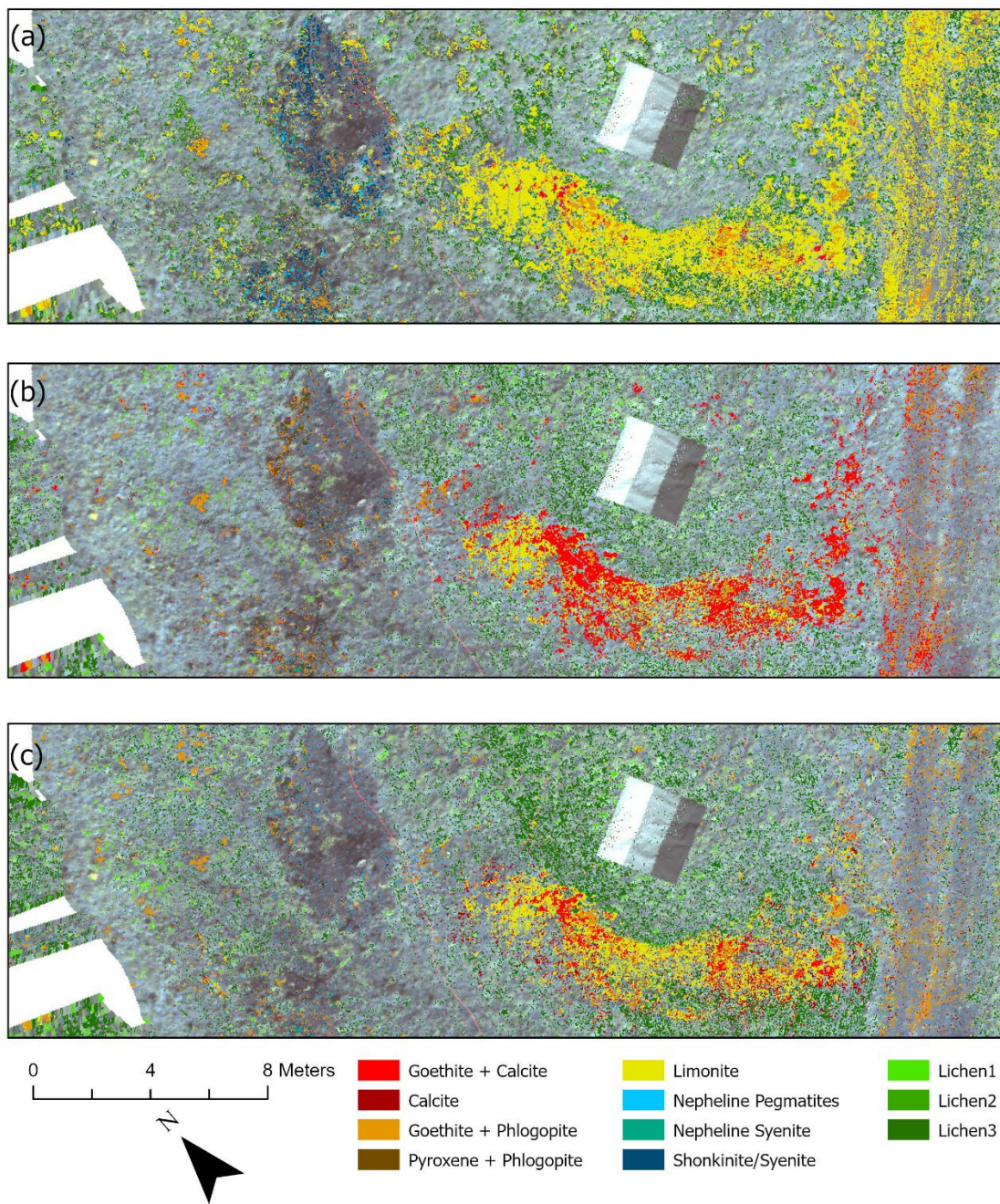


Figure 11: Classification results of Trench 2 of the 3-cm dataset using (a) the SAM, (b) the SID, and (c) the SID-SAM methods.

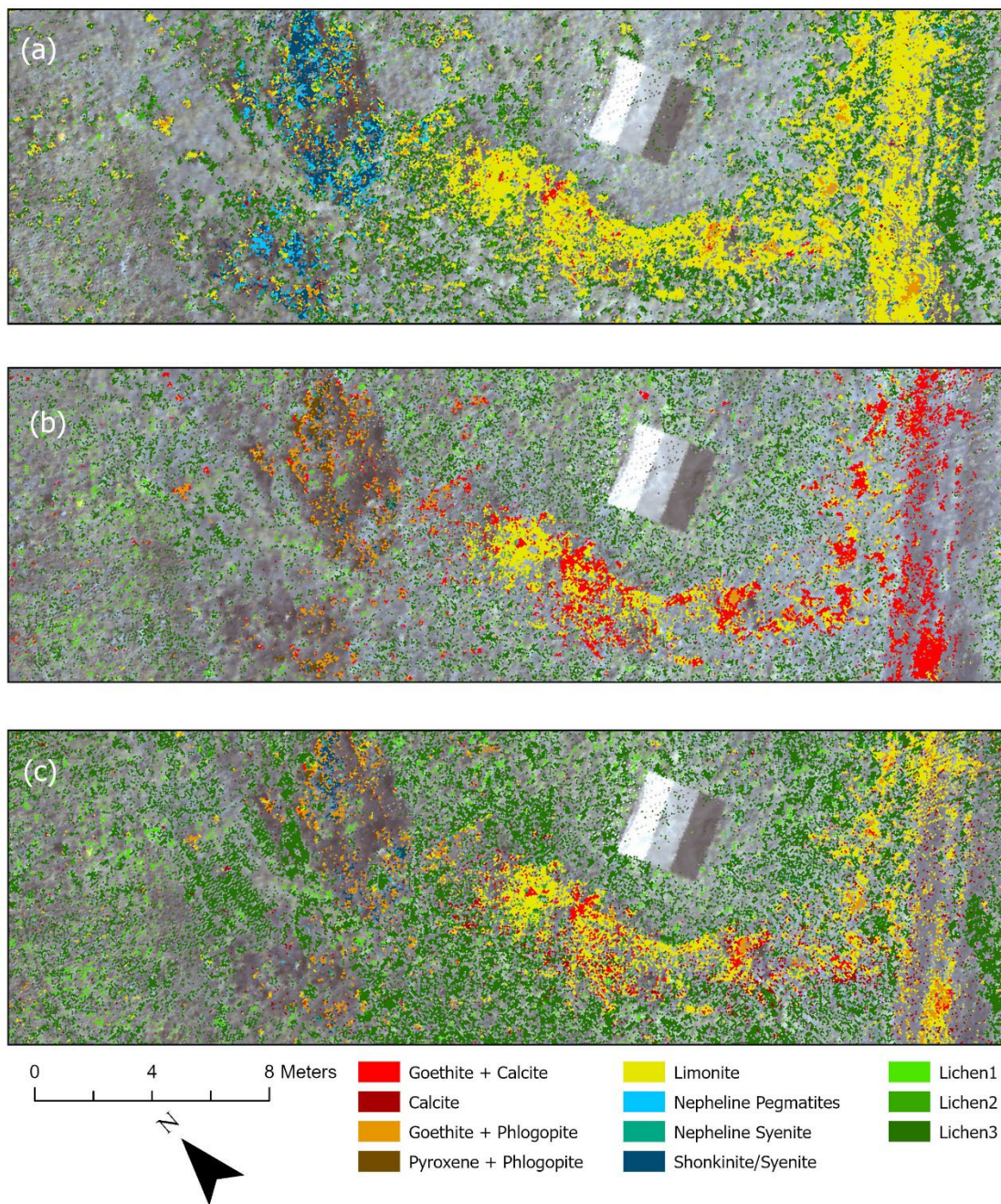


Figure 12: Classification results of Trench 2 of the 5-cm dataset using (a) the SAM, (b) the SID, and (c) the SID-SAM methods.

5. Discussion

This study used the radiometric signature of Th and hyperspectral results to delineate a prospective area of rare earth enrichment to add detailed mapping of the study area. Both remote

sensing methods provided results consistent with previous field geologic methods; gamma-ray data were consistent with scintillometer reading and soil sampling results from McNary (1981), and SAM and SID-SAM hyperspectral classification (Figure 11(a,c) and Figure 12(a,c)) correlate with historical surface geologic mapping (Figure 2). Hyperspectral results show the greatest distribution of carbonate minerals occurring within Trench 2. The geochemical analysis further validates the presence of rare earth elements in Trench 2 and shows the enrichment of rare earth elements in Trench 2 altered carbonate-rich material. The results of XRF showed that Trench 2 altered carbonate-rich material is enriched in La, Ce, and Th when compared to Trench 2 altered shonkinite material. The SEM-EDS results showed the presence of REE-carbonate minerals synchysite, bastnasite, and parisite. Trace amounts of thorium were found in the rare earth minerals within the altered carbonate-rich material through SEM-EDS analysis. Trench 2 was not formally defined as a carbonatite; however, these geochemical results support using carbonate and Th as indicators for rare earth enrichment in this study area. This study highlights the advantage of high-resolution remote sensing techniques to identify small areas (less than one meter) of carbonate mineralization associated with rare earth element enrichment, and these techniques could apply to other alkaline complexes to explore small-scale carbonatites and carbonate mineralization.

The biggest advantage of UAS-borne hyperspectral imaging is seen in the mapping of Trench 2. The alteration zone of Trench 2 is approximately 15 m x 2 m, and carbonate-rich veins are less than a meter wide. Airborne and satellite sensors such as AVIRIS, HyMap, Hyperion, Prisma, and EnMap collect data at meter to tens of meter pixel resolution, which lack the spatial resolution to map structures at the scale of Trench 2 with much detail. The UAS-borne

hyperspectral imaging from this study provided centimeter-scale mapping of small features that could be overlooked from lower-resolution platforms.

The methods presented here offer a potential workflow for UAS-assisted exploration. Gamma-ray spectroscopy could be flown first to define larger-scale areas of potential interest based on variations in Th, U, and K values. Next, hyperspectral imagery could be flown over the areas defined by gamma-ray spectroscopy, and the data could be analyzed for carbonate minerals. Finally, detailed maps produced from hyperspectral imaging could be used to guide hand sample collection in the field for further geochemical analysis.

Thorium results outline an area where one would most likely expect to find carbonate minerals associated with rare earth mineralization, and it would be less likely to find these minerals outside the defined area. Based on this assumption, the SAM method performed the best, as carbonate minerals were primarily distributed only within the defined area. Additionally, the SAM method showed the best distribution of shonkinite/syenite, nepheline syenite, and nepheline pegmatite consistent with the geologic map of Trench 2. The SID-SAM method also performed well, demonstrating thicker coverage of carbonate pixels in areas of known carbonate-oxide material within Trench 2. The results of the SID method showed the greatest distribution of carbonate minerals but disagreed with the geologic mapping, ground truth results, and Th results. It is important to note that each method used a different threshold, therefore it is difficult to compare the quantity of pixels classified. Instead, the evaluation is based on the quality of classification in comparison to gamma-ray spectroscopy results, historic geologic mapping, and ground truth sample collection.

One challenge of hyperspectral classification for mineral exploration was accurately differentiating rock types from weathered and lichen-covered outcrops. Geologic mapping and

ground truth results show that outcrops surrounding Trenches 2 and 3 are primarily shonkinite/syenite and nepheline syenite dikes. The SAM and SID-SAM methods classified these outcrops as limonite, goethite + phlogopite (weathering signatures), or lichen. As Section 2.1 noted, outcrops outside the trenches were weathered and covered in lichen. Aside from carbonate, the rocks formed from alkalic-carbonatite intrusions have few spectral features (Neave et al, 2016; Rowan et al., 1986). Weathered surfaces and lichen can change the spectral signatures of rocks and minerals depending on the extent of the weathering and thickness of lichen coverage (Rautianinen et al., 2024; Rollin et al., 1994), limiting the detection and mapping of the minerals they are encrusting. Several studies have used spectral mixture analysis (SMA) to overcome the challenges of using satellite- or manned aircraft-borne hyperspectral imagery in high-vegetated areas due to low spatial resolution of tens of meters (Zhang et al., 2005; Rivard et al., 2009; Morison et al., 2014). Centimeter-resolution imagery collected through UAS-borne hyperspectral sensors may help overcome the challenges of spectral mixing. However, considering the small scale of exposed minerals in outcrops, spectral unmixing methods might also be used to improve mineral identification and mapping at the centimeter level.

Another challenge was the background noise in the spectrum. In the hyperspectral imagery, the spectrum became noisier at the longer end of the wavelength range (>2000 nm). Though this is generally an issue for most SWIR spectrometers, this presents a significant limitation on the identification of relevant minerals —the diagnostic absorption bands for carbonate lie in the noisy wavelength range (2330 nm -2340 nm). Due to the low spectral reflectance of alkaline rocks, noise in the imaging spectra can cause misclassification using any of the three classification methods. The Savitsky-Golay filter smooths the imagery spectrum but comes at the expense of spectral resolution and does not remove the noise altogether.

The classification results of the 3-cm and 5-cm datasets differ only slightly. From a data collection standpoint, this is promising. Each dataset was collected using one set of batteries. The 5cm dataset was flown at 80 m and covered approximately $\sim 66,400 \text{ m}^2$, while the 3-cm dataset, flown at 60 m, covered just over half of the area, $\sim 34,867 \text{ m}^2$. The Headwall software calculates a recommended flight speed based on several factors, including exposure and height above ground. Though environmental factors out of our control determine exposure, flight height is within our control. Increasing height above ground decreases spatial resolution but allows for quicker flight speed and fewer lines flown, maximizing the area covered and battery life. In summary, decreased spatial resolution did not sacrifice the ability to classify carbonate signatures in small geologic structures in this study. Similar results between the two datasets could also indicate that spectral mixing is not as significant an issue at the cm scale. Instead, misclassification is more likely from noisy data and endmember reference spectra chosen for classification.

6. Conclusions

This study applied high-resolution SWIR imagery and gamma-ray spectroscopy to identify areas of interest for REE exploration by using carbonate and thorium as indicators. Additionally, this study looked at high-resolution SWIR imagery for mapping associated alkalic rocks, weathering signatures, and lichen. Though the Bearpaw Mountains and the Rocky Boy Stock have been focus areas for previous studies, this study adds to the limited body of research on the Bowery Peak prospects. It adds geochemical analysis of rock samples to identify rare earth elements in the Bowery Peak Prospects.

- SEM-EDS analysis of Trench 2 carbonate material identified the rare earth minerals parisite, bastnaesite, and synchysite. XRF and XRD results defined the composition

difference between two Trench 2 altered materials: altered shonkinite and carbonate material.

- The gamma-ray spectroscopy survey results, corroborated with historic soil/rock sampling and scintillometer readings, show an area of increased radiation around Trench 2 and to the southeast.
- The hyperspectral imagery SAM and SID-SAM classification results identified small areas (less than one meter) of carbonate mineralization within Trench 2 and Trench 3. Historic geologic mapping and geochemical analysis supported the results.

Results of UAS-borne gamma-ray spectroscopy and hyperspectral imagery complement each other. Gamma-ray spectroscopy defined a general area of interest and method for validating hyperspectral results, and hyperspectral imagery was used for detailed mapping. This study demonstrated a possible workflow for integrating UAS-borne geophysical data with traditional geological exploration methods. In the future, other methods of hyperspectral classification and integration of hyperspectral and gamma-ray data should be explored, such as machine learning and deep learning. UAS and geophysical sensor technology are quickly evolving; improvements in signal-to-noise ratios and hyperspectral sensor development allowing for the evaluation of the full VNIR/SWIR (400 nm - 25000 nm) will improve the classification of rare earth element carbonates by allowing researchers to evaluate Nd and carbonate absorption features.

7. References

- Barton, I.F., Gabriel, M.J., Lyons-Baral, J., Barton, M.D., Duplessis, L., Roberts, C., 2021. Extending geometallurgy to the mine scale with hyperspectral imaging: a pilot study using drone- and ground-based scanning. *Mining, Metallurgy & Exploration* 38, 799–818. <https://doi.org/10.1007/s42461-021-00404-z>
- Bedini, E., Rasmussen, T.M., 2018. Use of airborne hyperspectral and gamma-ray spectroscopy data for mineral exploration at the Sarfartoq carbonatite complex, southern West Greenland. *Geosci J* 22, 641–651. <https://doi.org/10.1007/s12303-017-0078-5>
- Bergantino, R.N., Porter, K.W., Carter Hearn, Jr, B., 2002. Geologic map of the Rocky Boy 30 x 60 minute quadrangle north-central Montana. Montana Bureau of Mines and Geology open-file report 451.
- Boesche, N., Rogass, C., Lubitz, C., Brell, M., Herrmann, S., Mielke, C., Tonn, S., Appelt, O., Altenberger, U., Kaufmann, H., 2015. Hyperspectral REE (Rare Earth Element) mapping of outcrops—applications for neodymium detection. *Remote Sensing* 7, 5160–5186. <https://doi.org/10.3390/rs70505160>
- Booyesen, R., Jackisch, R., Lorenz, S., Zimmermann, R., Kirsch, M., Nex, P.A.M., Gloaguen, R., 2020. Detection of REEs with lightweight UAV-based hyperspectral imaging. *Sci Rep* 10, 17450. <https://doi.org/10.1038/s41598-020-74422-0>
- Booyesen, Zimmermann, Lorenz, Gloaguen, Nex, Andreani, Möckel, 2019. Towards multiscale and multisource remote sensing mineral exploration using RPAS: A case study in the Lofdal Carbonatite-Hosted REE deposit, Namibia. *Remote Sensing* 11, 2500. <https://doi.org/10.3390/rs11212500>

- Chang, C.-I., 2004. New hyperspectral discrimination measure for spectral characterization. *Opt. Eng* 43, 1777. <https://doi.org/10.1117/1.1766301>
- Chein-I Chang, 2000. An information-theoretic approach to spectral variability, similarity, and discrimination for hyperspectral image analysis. *IEEE Trans. Inform. Theory* 46, 1927–1932. <https://doi.org/10.1109/18.857802>
- Chen, X., Warner, T.A., Campagna, D.J., 2010. Integrating visible, near-infrared and short-wave infrared hyperspectral and multispectral thermal imagery for geological mapping at Cuprite, Nevada: a rule-based system. *International Journal of Remote Sensing* 31, 1733–1752. <https://doi.org/10.1080/01431160902926616>
- Cloutis, E.A., 2002. Pyroxene reflectance spectra: Minor absorption bands and effects of elemental substitutions. *J.-Geophys.-Res.* 107. <https://doi.org/10.1029/2001JE001590>
- Golroudbary, S.R., Makarava, I., Kraslawski, A., Repo, E., 2022. Global environmental cost of using rare earth elements in green energy technologies. *Science of The Total Environment* 832, 155022. <https://doi.org/10.1016/j.scitotenv.2022.155022>
- Herrmann, S., 2019. Capacity of imaging spectroscopy for the characterisation of REO, REE bearing minerals and primary REE-deposits. Scientific Technical Report - Data; 19/08 26 MB. <https://doi.org/10.2312/GFZ.B103-19089>
- Jackisch, R., Lorenz, S., Kirsch, M., Zimmermann, R., Tusa, L., Pirttijärvi, M., Saartenoja, A., Ugalde, H., Madriz, Y., Savolainen, M., Gloaguen, R., 2020. Integrated geological and geophysical mapping of a carbonatite-hosting outcrop in Siilinjärvi, Finland, using unmanned aerial systems. *Remote Sensing* 12, 2998. <https://doi.org/10.3390/rs12182998>

- Kale, K.V., Solankar, M.M., Nalawade, D.B., Dhumal, R.K., Gite, H.R., 2017. A research review on hyperspectral data processing and analysis algorithms. *Proc. Natl. Acad. Sci., India, Sect. A Phys. Sci.* 87, 541–555. <https://doi.org/10.1007/s40010-017-0433-y>
- Kruse, F.A., Lefkoff, A.B., Boardman, J.W., Heidebrecht, K.B., Shapiro, A.T., Barloon, P.J., Goetz, A.F.H., 1993. The spectral image processing system (SIPS)—interactive visualization and analysis of imaging spectrometer data. *Remote Sensing of Environment* 44, 145–163. [https://doi.org/10.1016/0034-4257\(93\)90013-N](https://doi.org/10.1016/0034-4257(93)90013-N)
- Le Maitre, R.W., Streckeisen, A., Zanettin, B., Le Bas, M.J., Bonin, B., Bateman, P. (Eds.), 2002. *Igneous rocks: A classification and glossary of terms*, 2nd ed. Cambridge University Press, Cambridge. <https://doi.org/10.1017/CBO9780511535581>
- McNary, S.W., 1981. Field inventory of mineral resources on the Rocky Boy's Indian Reservation, Montana, Report BIA No. 34-II. U.S. Bureau of Mines.
- Morison, M., Cloutis, E., Mann, P., 2014. Spectral unmixing of multiple lichen species and underlying substrate. *International Journal of Remote Sensing* 35, 478–492. <https://doi.org/10.1080/01431161.2013.871085>
- Neave, D.A., Black, M., Riley, T.R., Gibson, S.A., Ferrier, G., Wall, F., Broom-Fendley, S., 2016. On the feasibility of imaging carbonatite-hosted rare earth Element deposits using remote sensing. *Economic Geology* 111, 641–665. <https://doi.org/10.2113/econgeo.111.3.641>
- Pecora, W.T., 1962. Carbonatite Problem in the Bearpaw Mountains, Montana, in: Engel, A.E.J., James, H.L., Leonard, B.F. (Eds.), *Petrologic Studies*. Geological Society of America, USA, pp. 83–104. <https://doi.org/10.1130/Petrologic.1962.83>

- Pecora, W.T., 1957. Preliminary geologic map of the Warrick quadrangle, Bearpaw Mountains, Montana. Miscellaneous geologic investigations; map I-237. <https://doi.org/10.3133/i237>
- Pecora, W.T., 1956. Carbonatites: A review. *Geol Soc America Bull* 67, 1537. [https://doi.org/10.1130/0016-7606\(1956\)67\[1537:CAR\]2.0.CO;2](https://doi.org/10.1130/0016-7606(1956)67[1537:CAR]2.0.CO;2)
- Pecora, W.T., 1942. Nepheline syenite pegmatites, Rocky Boy stock, Bearpaw Mountains, Montana. *The American Mineralogist* 27, 397–424.
- Peyghambari, S., Zhang, Y., 2021. Hyperspectral remote sensing in lithological mapping, mineral exploration, and environmental geology: an updated review. *J. Appl. Rem. Sens.* 15. <https://doi.org/10.1117/1.JRS.15.031501>
- Rautiainen, M., Kuusinen, N., Majasalmi, T., 2024. Remote sensing and spectroscopy of lichens. *Ecology and Evolution* 14, e11110. <https://doi.org/10.1002/ece3.11110>
- Rivard, B., Zhang, J., Feng, J., Sanchez-Azofeifa, G.A., 2009. Remote predictive lithologic mapping in the Abitibi Greenstone Belt, Canada, using airborne hyperspectral imagery. *Canadian Journal of Remote Sensing* 35, S95–S105. <https://doi.org/10.5589/m10-002>
- Rollin, E., Milton, E., Roche, P., 1994. The influence of weathering and lichen cover on the reflectance spectra of granitic rocks☆. *Remote Sensing of Environment* 50, 194–199. [https://doi.org/10.1016/0034-4257\(94\)90045-0](https://doi.org/10.1016/0034-4257(94)90045-0)
- Rowan, L.C., Bowers, T.L., Crowley, J.K., Anton-Pacheco, C., Gumiel, P., Kingston, M.J., 1995. Analysis of airborne visible-infrared imaging spectrometer (AVIRIS) data of the Iron Hill, Colorado, carbonatite-alkalic igneous complex. *Economic Geology* 90, 1966–1982. <https://doi.org/10.2113/gsecongeo.90.7.1966>

- Rowan, L.C., Kingston, M.J., Crowley, J.K., 1986. Spectral reflectance of carbonatites and related alkalic igneous rocks; selected samples from four North American localities. *Economic Geology* 81, 857–871. <https://doi.org/10.2113/gsecongeo.81.4.857>
- Sandino, J., Pegg, G., Gonzalez, F., Smith, G., 2018. Aerial mapping of forests affected by pathogens using UAVs, hyperspectral sensors, and artificial intelligence. *Sensors* 18, 944. <https://doi.org/10.3390/s18040944>
- Shives, R.B.K. 2015. Using gamma ray spectrometry to find rare metals. In: Simandl, G.J. and Neetz, M., (Eds.), *Symposium on Strategic and Critical Materials Proceedings*, November 13-14, 2015, Victoria, British Columbia. British Columbia Ministry of Energy and Mines, British Columbia Geological Survey Paper 2015-3, pp. 199-209.
- Simandl, G.J., Paradis, S., 2018. Carbonatites: related ore deposits, resources, footprint, and exploration methods. *Applied Earth Science* 127, 123–152. <https://doi.org/10.1080/25726838.2018.1516935>
- Van Gosen B.S., Verplanck P.L., Long K.R., Gambogi J., Seal II R.R., 2014. The rare-earth elements: Vital to modern technologies and lifestyles (USGS Numbered Series), Fact Sheet 2014-3078. U.S. Geological Survey, Reston, VA. <https://doi.org/10.3133/fs20143078>
- Vanegas, F., Bratanov, D., Powell, K., Weiss, J., Gonzalez, F., 2018. A novel methodology for improving plant pest surveillance in vineyards and crops using UAV-based hyperspectral and spatial Data. *Sensors* 18, 260. <https://doi.org/10.3390/s18010260>
- Zhang, J., Rivard, B., Sánchez-Azofeifa, A., 2005. Spectral unmixing of normalized reflectance data for the deconvolution of lichen and rock mixtures. *Remote Sensing of Environment* 95, 57–66. <https://doi.org/10.1016/j.rse.2004.11.019>

